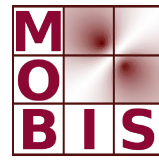




SpezialForschungsBereich F 32



Karl-Franzens Universität Graz  
Technische Universität Graz  
Medizinische Universität Graz



# Classical and all-floating FETI methods for the simulation of arterial tissues

Christoph M. Augustin    Gerhard A. Holzapfel  
Olaf Steinbach

SFB-Report No. 2013-012

September 2013

A-8010 GRAZ, HEINRICHSTRASSE 36, AUSTRIA

Supported by the  
Austrian Science Fund (FWF)

SFB sponsors:

- **Austrian Science Fund (FWF)**
- **University of Graz**
- **Graz University of Technology**
- **Medical University of Graz**
- **Government of Styria**
- **City of Graz**



# Classical and all-floating FETI methods for the simulation of arterial tissues

Christoph M. Augustin<sup>1,3,\*</sup>, Gerhard A. Holzapfel<sup>2,4</sup>, Olaf Steinbach<sup>1</sup>

<sup>1</sup>Institute of Computational Mathematics, Graz University of Technology,  
Steyrergasse 30, 8010 Graz, Austria

<sup>2</sup>Institute of Biomechanics, Center of Biomedical Engineering, Graz University of Technology,  
Kronesgasse 5, 8010 Graz, Austria

<sup>3</sup>Institute of Biophysics, Medical University of Graz, Harrachgasse 21, 8010 Graz, Austria

<sup>4</sup>Department of Solid Mechanics, School of Engineering Sciences, Royal Institute of Technology (KTH),  
Osquars Backe 1, 100 44 Stockholm, Sweden

## Abstract

High-resolution and anatomically realistic computer models of biological tissues play a significant role in the understanding of the function of cardiovascular components in health and disease. However, the computational effort to handle fine grids to resolve the geometries as well as sophisticated tissue models is very challenging. One possibility to derive a strongly scalable parallel solution algorithm is to consider finite element tearing and interconnecting (FETI) methods. In this study we propose and investigate the application of FETI methods to simulate the elastic behavior of biological tissues. As one particular example we choose the artery which is – as most other biological tissues – characterized by anisotropic and nonlinear material properties. We compare two specific approaches of FETI methods, classical and all-floating, and investigate the numerical behavior of different preconditioning techniques. In comparison to classical FETI, the all-floating approach has not only advantages concerning the implementation but in many cases also concerning the convergence of the global iterative solution method. This behavior is illustrated with numerical examples. We present results of linear elastic simulations to show convergence rates, as expected from the theory, and results from the more sophisticated nonlinear case where we apply a well-known anisotropic model to the realistic geometry of an artery. Although the FETI methods have a great applicability on artery simulations we will also discuss some limitations concerning the dependence on material parameters.

**Keywords.** artery, biological tissues, all-floating FETI, parallel computing

## 1 Introduction

The modeling of different elastic materials is realized by using a strain-energy function  $\Psi$ . For a comprehensive overview and the mathematical theory on elastic deformations, see [1, 2, 3, 4]. A well established model for arterial tissues was introduced by Holzapfel et al. [5, 6]. This model was further developed and enlarged to collagen fiber dispersion in [7, 8, 6]; see [9] for the modeling of residual stresses in arteries which play also an important role in tissue engineering. An adequate model for the myocardium can be found in [10]. The fine mesh structure to model

---

\*christoph.augustin@medunigraz.at; Corresponding author

cardiovascular organs normally results in a very large number of degrees of freedom (dof). The combination with the high complexity of the underlying partial differential equations demands fast solution algorithms and, conforming to up-to-date computer hardware architectures, parallel methods. One possibility to achieve these specifications are domain decomposition (DD) methods which acquired a lot of attention in the last years and resulted in the development of several overlapping as well as non-overlapping DD methods, see [11]. They all work according to the same principle: the computational domain  $\Omega$  is subdivided into a set of (overlapping or non-overlapping) subdomains  $\Omega_i$ . DD algorithms now decompose the large global problem into a set of smaller local problems on the subdomains, with suitable transmission or interface conditions. This yields a natural parallelization of the underlying problem. In addition to well established standard DD methods, other examples for more advanced domain decomposition methods are hybrid methods [12], mortar methods [13, 14, 15] and tearing and interconnecting methods [16].

In this paper we focus on the finite element tearing and interconnecting (FETI) method where the strategy is to decompose the computational domain into a finite number of non-overlapping subdomains. Therein the corresponding local problems can be handled efficiently by direct solvers. The reduced global system, that is related to discrete Lagrange multipliers on the interface, is then solved with a parallel Krylov space method to deduce the desired dual solution. This is, in the case of elasticity, the boundary stress and subsequently, in a postprocessing step, we compute the primal unknown, i.e. the displacements, locally. For the global Krylov space method, such as the conjugate gradient (CG) or the generalized minimal residual (GMRES) method, we need to have a suitable preconditioning technique. Here we consider a simple lumped preconditioner and an almost optimal Dirichlet preconditioner, as proposed by Farhat et al. [17].

A variant of the classical FETI method is the all-floating tearing and interconnecting approach (AF-FETI) where, in contrast to the classical approach, the Dirichlet boundary acts as a part of the interface. It was introduced independently for the boundary element method by Steinbach and Of [18, 19] and as the Total-FETI (TFETI) method for finite elements by Dostál et al. [20]. This approach shows advantages in the implementation and, due to mapping properties of the involved operators, improves the convergence of the global iterative method for the considered problems. This behavior is illustrated with numerical examples, which are – to the best of our knowledge – the first application of all-floating FETI method to nonlinear and anisotropic biological materials.

An essential part of FETI methods is solving the local subproblems. Challenges occur with so-called *floating subdomains* which have no contribution to the Dirichlet boundary. These cases correspond to local Neumann problems and the solutions are – in the case of elasticity – only unique up to the rigid body modes. One possibility to overcome this trouble is a modification of the classical approach, the dual-primal FETI (FETI-DP) method, cf. Farhat et al. [21] and Klawonn and Widlund [22]. In this variant some specific primal dof are fixed. This yields solvable systems for all subdomains. Choosing the primal dof may be very sophisticated [23]. This approach was already applied to model arterial tissues by Klawonn and Rheinbach, see, for example, [24, 25].

Both the classical FETI method, as well as all-floating FETI, needs the construction of a generalized inverse matrix. This may be achieved using direct solvers with a sparsity preserving stabilization or stabilized iterative methods. For a mathematical analysis of FETI methods, including convergence proofs for the classical one-level FETI method cf. [26, 22, 27].

## 2 Modeling Arterial Tissues

The deformation of a body  $\mathcal{B}$  is described by a function  $\phi : \Omega_0 \rightarrow \Omega_t$  with the *reference configuration*  $\Omega_0 \subset \mathbb{R}^3$  at time  $t = 0$  and the *current configuration*  $\Omega_t$  at time  $t > 0$ . With this we introduce the displacement field  $\mathbf{U}$  in the reference configuration and the displacement field  $\mathbf{u}$  in the current configuration,

$$\mathbf{x} = \phi(\mathbf{X}) = \mathbf{X} + \mathbf{U}(\mathbf{X}) \in \Omega_t, \quad \mathbf{X} = \phi^{-1}(\mathbf{x}) = \mathbf{x} - \mathbf{u}(\mathbf{x}) \in \Omega_0,$$

and the deformation gradient as, see, e.g., [2],

$$\mathbf{F} = \text{Grad } \phi(\mathbf{X}) = \mathbf{I} + \text{Grad } \mathbf{U}.$$

Moreover, we denote by  $J = \det \mathbf{F}$  the Jacobian of  $\mathbf{F}$  and by  $\mathbf{C} = \mathbf{F}^\top \mathbf{F}$  the right Cauchy–Green tensor. For later use, to model the nearly incompressible behavior of biological tissues, we introduce the following split of the deformation gradient in a volumetric and an isochoric part, compare Flory [28], i.e.

$$\mathbf{F} = J^{1/3} \bar{\mathbf{F}}, \quad \text{with } \det \bar{\mathbf{F}} = 1. \quad (1)$$

Consequently, this multiplicative split can be applied to other tensors such as the right Cauchy–Green tensor. Thus

$$\mathbf{C} = J^{2/3} \bar{\mathbf{C}}, \quad \text{with } \bar{\mathbf{C}} = \bar{\mathbf{F}}^\top \bar{\mathbf{F}} \text{ and } \det \bar{\mathbf{C}} = 1.$$

As a starting point for the modeling of biological tissues the stationary equilibrium equations in the current configuration are considered to find a displacement field  $\mathbf{u}$  according to

$$\text{div } \boldsymbol{\sigma}(\mathbf{u}, \mathbf{x}) + \mathbf{b}_t(\mathbf{x}) = \mathbf{0} \quad \text{for } \mathbf{x} \in \Omega_t, \quad (2)$$

where  $\boldsymbol{\sigma}(\mathbf{u}, \mathbf{x})$  is the Cauchy stress tensor and  $\mathbf{b}_t(\mathbf{x})$  is the body force at time  $t$ .

In addition, we incorporate boundary conditions to describe displacements or normal stresses on the boundary  $\Gamma_t = \partial\Omega_t$ , which is decomposed into disjoint parts such that  $\partial\Omega_t = \bar{\Gamma}_{t,D} \cup \bar{\Gamma}_{t,N}$ . Dirichlet boundary conditions on  $\Gamma_{t,D}$  correspond to a given displacement field  $\mathbf{u} = \mathbf{u}_D(\mathbf{x})$ , while Neumann boundary conditions on  $\Gamma_{t,N}$  are identified physically with a given surface traction  $\boldsymbol{\sigma}(\mathbf{u}, \mathbf{x}) \mathbf{n}_t(\mathbf{x}) = \mathbf{g}_t(\mathbf{x})$ , where  $\mathbf{n}_t(\mathbf{x})$  denotes the exterior normal vector at time  $t$ .

The equilibrium equations and the boundary conditions may also be formulated in terms of the reference configuration, i.e.

$$\text{Div } \mathbf{F}\mathbf{S}(\mathbf{U}, \mathbf{X}) + \mathbf{b}_0(\mathbf{X}) = \mathbf{0} \quad \text{for } \mathbf{X} \in \Omega_0, \quad (3)$$

$$\mathbf{U}(\mathbf{X}) = \mathbf{U}_D(\mathbf{X}) \quad \text{for } \mathbf{X} \in \Gamma_{0,D}, \quad (4)$$

$$\mathbf{F}\mathbf{S}(\mathbf{U}, \mathbf{X})\mathbf{N}_0(\mathbf{X}) = \mathbf{G}_0(\mathbf{X}) \quad \text{for } \mathbf{X} \in \Gamma_{0,N}, \quad (5)$$

where  $\mathbf{S}$  is the second Piola–Kirchhoff tensor and  $\mathbf{b}_0(\mathbf{X})$  is the body force at time  $t = 0$ . In order to formulate the boundary conditions we introduce a prescribed displacement field  $\mathbf{U}_D(\mathbf{X})$ , the exterior normal vector  $\mathbf{N}_0(\mathbf{X})$  and the surface traction  $\mathbf{G}_0(\mathbf{X})$  in the reference configuration.

Considering the study of the properties of soft biological tissue we have to deal with a nonlinear relationship between stress and strain, with large deformations and an anisotropic material. Since linear elasticity models are not adequate for treating such a complex behavior, we take a look at the more general concept of nonlinear elasticity.

The nonlinear stress–strain response is modeled via a constitutive equation that links the stress to a derivative of a strain–energy function  $\Psi$ , representing the elastic stored energy per

unit reference volume. Derived from the Clausius–Duhem inequality, see [29, 30], we formulate the constitutive equations as

$$\boldsymbol{\sigma} = 2J^{-1}\mathbf{F}\frac{\partial\Psi(\mathbf{C})}{\partial\mathbf{C}}\mathbf{F}^\top \quad \text{and} \quad \mathbf{S} = 2\frac{\partial\Psi(\mathbf{C})}{\partial\mathbf{C}}.$$

We make use of the Rivlin–Ericksen representation theorem [31] and its extension to anisotropic materials, cf. [32], to find a representation of the strain-energy function  $\Psi$  in terms of the principal invariants of  $\mathbf{C}$ .

Arteries are vessels that transport blood from the heart to the organs. In vivo the artery is a prestretched material under an internal pressure load. Healthy arteries are highly deformable composite structures and show a nonlinear stress–strain response with a typical stiffening effect at higher pressures. Reasons for this are the embedded collagen fibers which lead to an anisotropic mechanical behavior of arterial walls. We denote by  $\mathbf{a}_{0,1}$  and by  $\mathbf{a}_{0,2}$  the predominant collagen fiber directions. An important observation is that arteries do not change their volume within the physiological range of deformation, hence they are treated as a nearly incompressible material, see, e.g., [5]. In this work we focus on the in vitro passive behavior of the healthy artery, see Fig. 1.

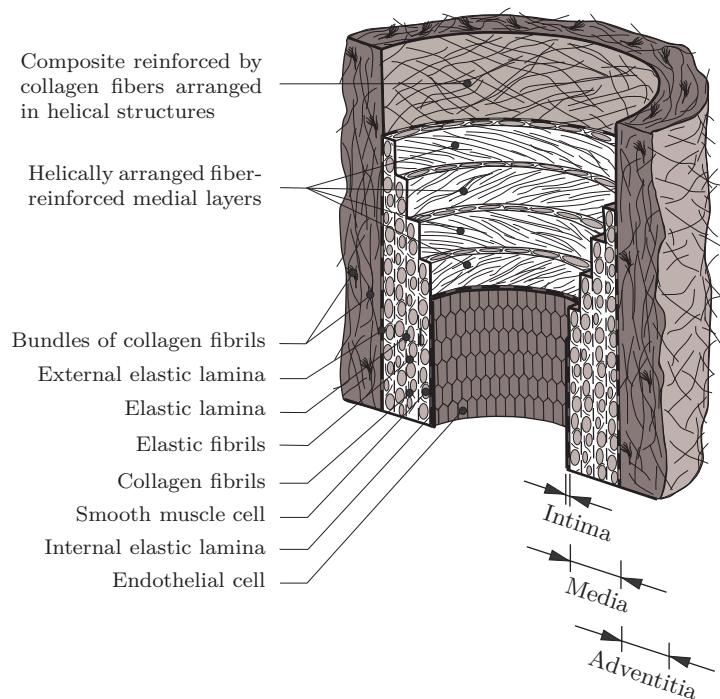


Figure 1: Diagrammatic model of the major components of a healthy elastic artery, from [5]. The intima, the innermost layer is negligible for the modeling of healthy arteries, it plays a very important role in the modeling of diseased arteries, though. The two predominant axial directions of the collagen fibers in the media and the adventitia are indicated with black lines.

To capture the nearly incompressibility condition we remember the decomposition (1), which yields an additive split of the strain–energy function into a so-called volumetric and an isochoric part, i.e.

$$\Psi(\mathbf{C}) = \Psi_{\text{vol}}(J) + \bar{\Psi}(\bar{\mathbf{C}}). \quad (6)$$

This procedure leads to constitutive equations in which the stress tensors are also additively decomposed into a volumetric and an isochoric part, i.e., cf. [2],

$$\boldsymbol{\sigma} = p\mathbf{I} + 2J^{-1}\mathbf{F}\frac{\partial\bar{\Psi}(\bar{\mathbf{C}})}{\partial\mathbf{C}}\mathbf{F}^\top \quad \text{and} \quad \mathbf{S} = Jp\mathbf{C}^{-1} + 2\frac{\partial\bar{\Psi}(\bar{\mathbf{C}})}{\partial\mathbf{C}}. \quad (7)$$

Here, the scalar-valued hydrostatic pressure is defined as

$$p := \frac{\partial\Psi_{\text{vol}}(J)}{\partial J}. \quad (8)$$

To capture the specifics of this fiber-reinforced composite, Holzapfel et al. [5] proposed an additional split of the isochoric strain-energy function  $\bar{\Psi}$  into an isotropic and an anisotropic part. Hence, the complete energy function can be written as

$$\Psi(\mathbf{C}) = \Psi_{\text{vol}}(J) + \bar{\Psi}_{\text{iso}}(\bar{\mathbf{C}}) + \bar{\Psi}_{\text{aniso}}(\bar{\mathbf{C}}, \mathbf{a}_{1,0}) + \bar{\Psi}_{\text{aniso}}(\bar{\mathbf{C}}, \mathbf{a}_{2,0}). \quad (9)$$

Following the classical approach we describe the volume changing part by

$$\Psi_{\text{vol}}(J) = \frac{\kappa}{2}(J-1)^2, \quad (10)$$

where  $\kappa > 0$ , which is comparable to the bulk modulus in linear elasticity, serves as a penalty parameter to enforce the incompressibility constraint.

To model the isotropic ground substance the classical neo-Hookean model, see, e.g., Ogden [4], is used. Thus

$$\bar{\Psi}_{\text{iso}}(\bar{\mathbf{C}}) = \frac{c}{2}(\bar{I}_1 - 3), \quad (11)$$

where  $c > 0$  is a stress-like material parameter and  $\bar{I}_1 = \text{tr}(\bar{\mathbf{C}})$  is the first principal invariant of the isochoric part of the right Cauchy-Green tensor. In (9),  $\bar{\Psi}_{\text{aniso}}$  is associated with the deformation in the direction of the collagen fibers. According to [5], this transversely isotropic response is described by

$$\bar{\Psi}_{\text{aniso}}(\bar{\mathbf{C}}, \mathbf{a}_{1,0}) = \frac{k_1}{2k_2} \{ \exp[k_2(\bar{I}_4 - 1)^2] - 1 \}, \quad (12)$$

$$\bar{\Psi}_{\text{aniso}}(\bar{\mathbf{C}}, \mathbf{a}_{2,0}) = \frac{k_1}{2k_2} \{ \exp[k_2(\bar{I}_6 - 1)^2] - 1 \}, \quad (13)$$

with the invariants  $\bar{I}_4 := \mathbf{a}_{1,0} \cdot (\bar{\mathbf{C}}\mathbf{a}_{1,0})$ ,  $\bar{I}_6 := \mathbf{a}_{2,0} \cdot (\bar{\mathbf{C}}\mathbf{a}_{2,0})$  and the material parameters  $k_1$  and  $k_2$ , which are both assumed to be positive. It is worth to mention that for the anisotropic responses (12) and (13) only contribute for the cases  $\bar{I}_4 > 1$  or  $\bar{I}_6 > 1$ , respectively. This condition is explained with the wavy structure of the collagen fibers, which are regarded as not being able to support compressive stresses. Thus, the fibers are assumed to be active in extension ( $\bar{I}_i > 1$ ) and inactive in compression ( $\bar{I}_i < 1$ ). This assumption is not only based on physical reasons but it is also essential for reasons of stability, see Holzapfel et al. [33].

The material parameters can be fitted to an experimentally observed response of the biological tissue. Following [5] we use the material parameters summarized in Table 1.

Similar models can also be used for the description of other biological materials, e.g., for the myocardium, cf. [10].

Table 1: Material parameters used in the numerical experiments; parameters taken from [5].

$c = 3.0$ kPa	$k_1 = 2.3632$ kPa	$k_2 = 0.8393$ (-)
---------------	--------------------	--------------------

### 3 Finite Element Approximation

#### 3.1 Variational formulation of nonlinear elasticity problems

In this section we consider the variational formulation of the equilibrium equations (2) and (3) with the corresponding Dirichlet and Neumann boundary conditions. In particular, using spatial coordinates, we have to find  $\mathbf{u} \in [H^1(\Omega_t)]^3$ ,  $\mathbf{u} = \mathbf{u}_D$  on  $\Gamma_{t,D}$ , such that

$$\langle \mathcal{A}_t(\mathbf{u}), \mathbf{v} \rangle_{\Omega_t} := \int_{\Omega_t} \boldsymbol{\sigma}(\mathbf{u}) : \boldsymbol{\varepsilon}(\mathbf{v}) \, d\mathbf{x} = \int_{\Omega_t} \mathbf{b}_t \cdot \mathbf{v} \, d\mathbf{x} + \int_{\Gamma_{t,N}} \mathbf{g}_t \cdot \mathbf{v} \, ds_{\mathbf{x}} =: \langle \mathcal{F}, \mathbf{v} \rangle_{\Omega_t} \quad (14)$$

is satisfied for all test functions  $\mathbf{v} \in [H^1(\Omega_t)]^3$ ,  $\mathbf{v} = \mathbf{0}$  on  $\Gamma_{t,D}$  and

$$\boldsymbol{\varepsilon}(\mathbf{v}) = \frac{1}{2} (\text{grad } \mathbf{v} + (\text{grad } \mathbf{v})^\top).$$

In (14),  $\mathcal{A}_t$  is the nonlinear operator in the current configuration which is induced by the stress tensor representation (7), and by using the related duality pairing  $\langle \cdot, \cdot \rangle_{\Omega_t}$ . For later use, we introduce the corresponding terms in the reference configuration  $\Omega_0$  as  $\langle \mathcal{A}_0(\mathbf{U}), \mathbf{V} \rangle_{\Omega_0}$  and  $\langle \mathcal{F}_0, \mathbf{V} \rangle_{\Omega_0}$ . Note that (14) formally corresponds to a variational formulation in linear elasticity. However, the integral and the involved terms have to be evaluated in the current configuration which comprises the nonlinearity of the system. If the test function  $\mathbf{v}$  is interpreted as the spatial velocity gradient, then  $\boldsymbol{\varepsilon}(\mathbf{v})$  is the rate of deformation tensor so that  $\langle \mathcal{A}_t(\mathbf{u}), \mathbf{v} \rangle_{\Omega_t}$  has the physical interpretation of the rate of internal mechanical work.

In terms of the reference configuration we seek the displacement field  $\mathbf{U} \in [H^1(\Omega_0)]^3$ ,  $\mathbf{U} = \mathbf{U}_D$  on  $\Gamma_{0,D}$ , such that

$$\langle \mathcal{A}_0(\mathbf{U}), \mathbf{V} \rangle_{\Omega_0} = \int_{\Omega_0} \mathbf{S}(\mathbf{U}) : \boldsymbol{\Sigma}(\mathbf{U}, \mathbf{V}) \, d\mathbf{X} = \int_{\Omega_0} \mathbf{b}_0 \cdot \mathbf{V} \, d\mathbf{X} + \int_{\Gamma_{0,N}} \mathbf{G}_0 \cdot \mathbf{V} \, ds_{\mathbf{X}} = \langle \mathcal{F}_0, \mathbf{V} \rangle_{\Omega_0} \quad (15)$$

is satisfied for all  $\mathbf{V} \in [H^1(\Omega_0)]^3$ ,  $\mathbf{V} = \mathbf{0}$  on  $\Gamma_{0,D}$ . In (15) we use the definition of the directional derivative of the Green–Lagrange strain tensor, i.e.

$$\boldsymbol{\Sigma}(\mathbf{U}, \mathbf{V}) = \frac{1}{2} \left( \text{Grad}^\top \mathbf{V} \mathbf{F}(\mathbf{U}) + \mathbf{F}^\top(\mathbf{U}) \text{Grad } \mathbf{V} \right),$$

which is also known as the variation or the material time derivative of the Green–Lagrange strain tensor in the literature.

It is important to note that results on existence of solutions in nonlinear elasticity can be stated given a polyconvex strain–energy function  $\Psi$ . For more details we refer to the results of Ball [34, 35], see also [1, 36] and Balzani et al. [37].

#### 3.2 Linearization and discretization

In the following we confine ourselves to the reference configuration  $\Omega_0$ . The formulations in the current configuration  $\Omega_t$  can be deduced in an analogous way.

For the computational domain  $\Omega_0 \subset \mathbb{R}^3$  we consider an admissible decomposition into  $N$  tetrahedral shape regular finite elements  $\tau_\ell$  of mesh size  $h_\ell$ , i.e.  $\bar{\Omega}_0 = \bar{\mathcal{T}}_N = \bigcup_{\ell=1}^N \bar{\tau}_\ell$ , and we introduce a conformal finite element space  $X_h \subset [H^1(\Omega_0)]^3$ ,  $M = \dim X_h$ , of piecewise polynomial continuous basis functions  $\varphi_i$ . Then the Galerkin finite element discretization of the variational formulation (15) results in a nonlinear system of algebraic equations to find  $\mathbf{U}_h \in X_h$  satisfying an approximate Dirichlet boundary condition  $\mathbf{U}_h = \mathbf{U}_{D,h}$  on  $\Gamma_{0,D}$  and

$$\langle \mathcal{A}_0(\mathbf{U}_h), \mathbf{V}_h \rangle_{\Omega_0} = \langle \mathcal{F}_0, \mathbf{V}_h \rangle_{\Omega_0} \quad (16)$$

for all  $\mathbf{V}_h \in X_h$ ,  $\mathbf{V}_h = 0$  on  $\Gamma_{0,D}$ . Note that  $\mathbf{U}_{D,h} \in X_h|_{\Gamma_{0,D}}$  denotes a suitable approximation of the given displacement  $\mathbf{U}_D$ .

For the solution of the nonlinear system (16) we apply Newton's method to obtain the recursion

$$\langle \Delta \mathbf{U}_h, \mathcal{A}'_0(\mathbf{U}_h^k) \mathbf{V}_h \rangle_{\Omega_0} = \langle \mathcal{F}_0, \mathbf{V}_h \rangle_{\Omega_0} - \langle \mathcal{A}_0(\mathbf{U}_h^k), \mathbf{V}_h \rangle_{\Omega_0}, \quad \mathbf{U}_h^{k+1} = \mathbf{U}_h^k + \Delta \mathbf{U}_h, \quad (17)$$

with the displacement field of the  $k$ -th Newton step  $\mathbf{U}_h^k$ , the increment  $\Delta \mathbf{U}_h$  and a suitable initial guess. For the computation of the tangential term  $\mathcal{A}'_0(\mathbf{U}_h^k)$  we need to evaluate

$$\begin{aligned} \langle \Delta \mathbf{U}_h, \mathcal{A}'_0(\mathbf{U}_h^k) \mathbf{V}_h \rangle_{\Omega_0} &= \int_{\Omega_0} \text{Grad}(\Delta \mathbf{U}_h) \mathbf{S}(\mathbf{U}_h^k) : \text{Grad} \mathbf{V}_h \, d\mathbf{X} \\ &+ \int_{\Omega_0} \mathbf{F}^\top \text{Grad} \Delta \mathbf{U}_h : \mathbb{C}(\mathbf{U}_h^k) : \mathbf{F}^\top \text{Grad}(\mathbf{V}_h) \, d\mathbf{X}. \end{aligned} \quad (18)$$

For a more detailed presentation how to compute the tangential term, in particular the fourth-order elasticity tensor  $\mathbb{C}(\mathbf{U}_h^k)$  we refer to [38, 39].

Note that the convergence rate of the Newton method is dependent on the initial guess, on the parameters used in the model and on the inhomogeneous Dirichlet and Neumann boundary conditions which influence  $\mathcal{F}_0$ .

In a time-stepping scheme we use zero for the initial guess, and the result of the  $k$ -th time-step as initial solution for the next step. The initial guess may also be the solution of a modified nonlinear elasticity problem such as the solution of the same nonlinear model but with modified parameters, e.g., a reduced penalty parameter  $\kappa$ , or modified boundary conditions, e.g., a reduced pressure on the surface. The latter is equivalent to an incremental load stepping scheme with a parameter  $\tau \in (0, 1]$ ,  $\tau \rightarrow 1$ , so that

$$\langle \Delta \mathbf{U}_h, \mathcal{A}'(\mathbf{U}_h^k) \mathbf{V}_h \rangle_{\Omega_0} = \langle \tau \mathcal{F}_0, \mathbf{V}_h \rangle_{\Omega_0} - \langle A(\mathbf{U}_h^k), \mathbf{V}_h \rangle_{\Omega_0}, \quad \mathbf{U}_h^{k+1} = \mathbf{U}_h^k + \Delta \mathbf{U}_h. \quad (19)$$

The standard finite element method (FEM) now yields a linear system of equations which is equivalent to the discretized variational formulation (17). Finally, we have to solve

$$\mathbf{K}'(\underline{U}^k) \Delta \underline{U} = \underline{\mathcal{F}} - \underline{K}(\underline{U}^k), \quad \underline{U}^{k+1} = \underline{U}^k + \Delta \underline{U}, \quad (20)$$

with the solution vector  $\underline{U}^k$  in the  $k$ -th Newton step and the increment  $\Delta \underline{U}$ . The tangent stiffness matrix  $\mathbf{K}'$  is calculated according to

$$\mathbf{K}'(\underline{U}^k)[i, j] := \langle \varphi_j, \mathcal{A}'(\mathbf{U}_h^k) \varphi_i \rangle_{\Omega_0},$$

and the terms of the right hand side are constructed by

$$\underline{\mathcal{F}}[i] := \langle \mathcal{F}_0, \varphi_i \rangle_{\Omega_0} \quad \text{and} \quad \underline{K}(\underline{U}^k)[i] := \langle A(\mathbf{U}_h^k), \varphi_i \rangle_{\Omega_0}.$$

The additive split of the stress tensors (7) and the introduction of the hydrostatic pressure (8) leads to the additional equation

$$p - \frac{\partial \Psi_{\text{vol}}(J)}{\partial J} = 0, \quad (21)$$

which has to be satisfied in a weak sense. For this we use the idea of *static condensation* where this volumetric variable is eliminated element-wise, see [39]. This may be achieved in using discontinuous basis functions; in this paper we will concentrate on piecewise constants. In the case of tetrahedral elements, this approach leads to  $\mathcal{P}_k$ - $\mathcal{P}_0$ -elements. Here  $k$  is the order of the basis functions for the displacement field. It is known that linear finite elements are very prone to volumetric locking. Hence, for nearly incompressible materials piecewise quadratic elements

( $k = 2$ ) are a better choice. The resulting  $P_2$ - $P_0$ -element is also the choice to model nearly incompressible arterial materials in [24] and is, in contrast to the widely used  $P_1$ - $P_0$ -element, stable for the nearly incompressible linear elasticity problem, e.g., see Boffi et al. [40]. For the numerical results in this work (Sect. 5) we use both linear ( $P_1$ - $P_0$ -element) and quadratic ( $P_2$ - $P_0$ -element) ansatz functions for the displacement field and compare the results.

Note that due to the symmetry of the stress tensor  $\mathbf{S}$  and the major and minor symmetry properties of the elasticity tensor  $\mathbb{C}$  the operator  $A'(\mathbf{U}^k)$  is self-adjoint. We can also show, using the positive definiteness of the elasticity tensor, see [4], and the polyconvexity of the strain-energy function (Sect. 3.1), that this operator is  $[H_0^1(\Omega_0, \Gamma_{0,D})]^3$ -elliptic and bounded, see [38, 4]. With these properties of the operator  $A'(\mathbf{U}_h^k)$  we can state that the linearized system (17)–(18) admits a unique solution  $\Delta \mathbf{U}_h$ . Furthermore, the tangent stiffness matrix  $\mathbf{K}'$  is symmetric and positive definite.

Simulations with large deformations and the hence required derivative of the Neumann boundary conditions (5) would yield an additional unsymmetric mass matrix on the left hand side of (20). To stay with an symmetric system we neglect this matrix but compensate it with a surface update of the geometry after each Newton step. Thus, our whole system is symmetric and we can use the conjugate gradient (CG) method as an iterative solver. Nonetheless, the FETI methods described in Sect. 4 also work for unsymmetric systems by using the GMRES method.

## 4 Finite Element Tearing and Interconnecting

To solve the linearized equations (20) arising in the Newton method we apply the finite element tearing and interconnecting approach [16], see also [24, 41, 42], and references given therein. The derivation of the FETI system for nonlinear mechanics will be performed in the reference configuration. In an analogous way this is also valid for the formulation in the current configuration. For a bounded domain  $\Omega_0 \subset \mathbb{R}^3$  we introduce a non-overlapping domain decomposition

$$\bar{\Omega}_0 = \bigcup_{i=1}^p \bar{\Omega}_{0,i} \quad \text{with } \Omega_{0,i} \cap \Omega_{0,j} = \emptyset \quad \text{for } i \neq j, \quad \Gamma_{0,i} = \partial\Omega_{0,i}, \quad (22)$$

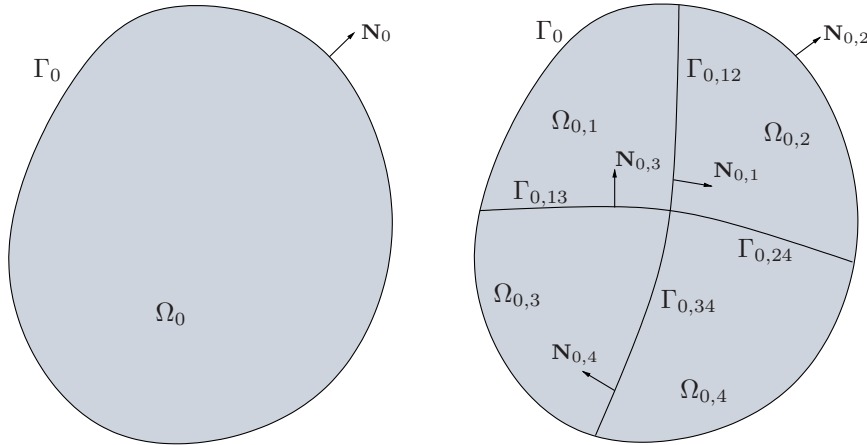


Figure 2: Decomposition of a domain  $\Omega_0$  into four subdomains  $\Omega_{0,i}$ .

see Fig. 2. The local interfaces are given by  $\Gamma_{0,ij} := \Gamma_{0,i} \cap \Gamma_{0,j}$  for all  $i < j$ . The skeleton of the domain decomposition (22) is denoted as

$$\Gamma_{0,C} := \bigcup_{i=1}^p \Gamma_{0,i} = \Gamma_0 \cup \bigcup_{i < j} \bar{\Gamma}_{0,ij}. \quad (23)$$

We assume that the finite element mesh  $\mathcal{T}_N$  matches the domain decomposition (22), i.e., we can reorder the degrees of freedom to rewrite the linear system (20) as

$$\begin{pmatrix} \mathbf{K}'_{11}(\underline{U}_1) & & & \mathbf{K}'_{1C}(\underline{U}_1)\mathbf{A}_1 \\ & \ddots & & \vdots \\ & & \mathbf{K}'_{pp}(\underline{U}_p) & \mathbf{K}'_{pC}(\underline{U}_p)\mathbf{A}_p \\ \mathbf{A}_1^\top \mathbf{K}'_{C1}(\underline{U}_1) & \cdots & \mathbf{A}_p^\top \mathbf{K}'_{Cp}(\underline{U}_p) & \sum_{i=1}^p \mathbf{A}_i^\top \mathbf{K}'_{CC}(\underline{U}_i)\mathbf{A}_i \end{pmatrix} \begin{pmatrix} \Delta \underline{U}_{1,I} \\ \vdots \\ \Delta \underline{U}_{p,I} \\ \Delta \underline{U}_C \end{pmatrix} = - \begin{pmatrix} \underline{K}_1(\underline{U}_1) \\ \vdots \\ \underline{K}_p(\underline{U}_p) \\ \sum_{i=1}^p \mathbf{A}_i^\top \underline{K}_C(\underline{U}_i) \end{pmatrix}, \quad (24)$$

where the increments  $\Delta \underline{U}_{i,I}^k$ , the stiffness matrices  $\mathbf{K}'_{ii}(\underline{U}_i^k)$  and the terms on the right hand side  $\underline{K}_i(\underline{U}_i^k)$ ,  $i = 1, \dots, p$ , are related to the local degrees of freedom within the subdomain  $\Omega_{0,i}$ . All terms with an index C correspond to degrees of freedom on the coupling boundary  $\Gamma_{0,C}$ , see (23), while  $\mathbf{A}_i$  denote simple reordering matrices taking boolean values.

#### 4.1 Classical FETI method

Starting from (24), the *tearing* is now carried out by

$$\Delta \underline{U}_i = \begin{pmatrix} \Delta \underline{U}_{i,I}^k \\ \mathbf{A}_i \Delta \underline{U}_C^k \end{pmatrix}, \quad \mathbf{K}'_i = \begin{pmatrix} \mathbf{K}'_{ii}(\underline{U}_i^k) & \mathbf{K}'_{iC}(\underline{U}_i^k) \\ \mathbf{K}'_{Ci}(\underline{U}_i^k) & \mathbf{K}'_{CC}(\underline{U}_i^k) \end{pmatrix}, \quad \underline{f}_i = - \begin{pmatrix} \underline{K}_i(\underline{U}_i^k) \\ \underline{K}_C(\underline{U}_i^k) \end{pmatrix},$$

where  $\mathbf{A}_i \Delta \underline{U}_C^k$  is related to degrees of freedom on the coupling boundary  $\Gamma_{0,i} \setminus \Gamma_0$ . As the unknowns  $\Delta \underline{U}_i$  are typically not continuous over the interfaces we have to ensure the continuity of the solution on the interface, i.e.

$$\Delta \underline{U}_i = \Delta \underline{U}_j \quad \text{on } \Gamma_{0,ij}, \quad i, j = 1, \dots, p. \quad (25)$$

This is done by applying the *interconnecting*

$$\sum_{i=1}^p \mathbf{B}_i \Delta \underline{U}_i = \underline{0}, \quad (26)$$

where the matrices  $\mathbf{B}_i$  are constructed from  $\{0, 1, -1\}$  such that (25) holds. By using discrete Lagrange multipliers  $\underline{\lambda}$  to enforce the constraint (26) we finally have to solve the linear system

$$\begin{pmatrix} \mathbf{K}'_1 & & & \mathbf{B}_1^\top \\ & \ddots & & \vdots \\ & & \mathbf{K}'_p & \mathbf{B}_p^\top \\ \mathbf{B}_1 & \cdots & \mathbf{B}_p & \mathbf{0} \end{pmatrix} \begin{pmatrix} \Delta \underline{U}_1 \\ \vdots \\ \Delta \underline{U}_p \\ \underline{\lambda} \end{pmatrix} = \begin{pmatrix} \underline{f}_1 \\ \vdots \\ \underline{f}_p \\ \underline{0} \end{pmatrix}. \quad (27)$$

## 4.2 All-floating FETI method

The idea of this special FETI method, cf., e.g., Of and Steinbach [19], is to treat all subdomains as floating subdomains, i.e. domains with no Dirichlet boundary conditions. In addition to the standard procedure of ‘gluing’ the subregions along the auxiliary interfaces, the Lagrange multipliers are now also used for the implementation of the Dirichlet boundary conditions, see Fig. 3. This simplifies the implementation of the FETI procedure since it is possible to treat all subdomains the same way. In addition, some tests (Sect. 5) show more efficiency than the classical FETI approach and the asymptotic behavior improves. This is due to the mapping properties of the Steklov–Poincaré operator, see [19, Remark 1]. The drawback is an increasing number of degrees of freedom and Lagrange multipliers. Compare also to Dostál et al. [20] for the related Total-FETI method. If all regions are treated as floating subdomains the conformance

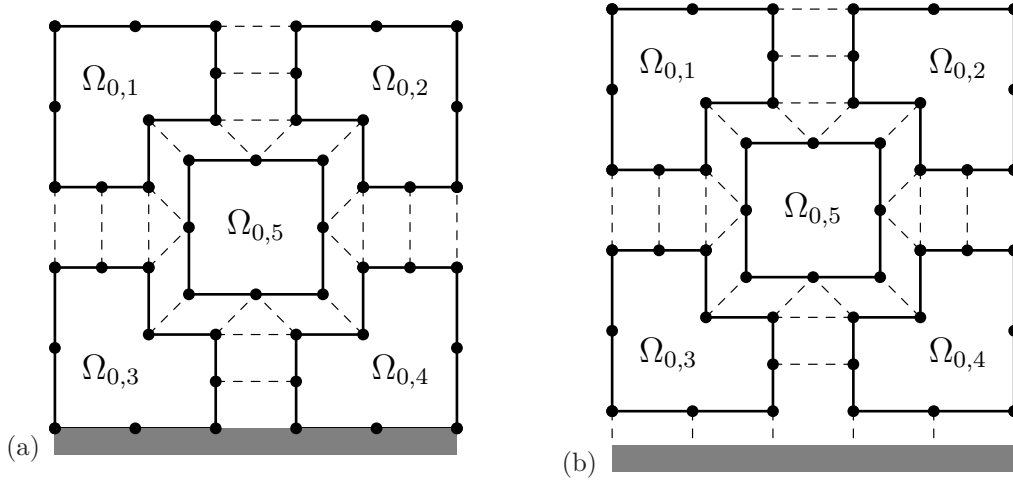


Figure 3: Fully redundant classical FETI (a) and all-floating FETI (b) formulation:  $\Omega_{0,i}$ ,  $i = 1, \dots, 5$ , denote the local subdomains, the black dots correspond to the subdomain vertices and the dashed lines correspond to the constraints (25). The gray strip indicates Dirichlet boundary conditions. Note that the number of constraints for the all-floating approach rises with the number of vertices on the Dirichlet boundary.

of the Dirichlet boundary conditions is not given; they have to be enhanced in the system of constraints using the slightly modified interconnecting

$$\sum_{i=1}^p \tilde{\mathbf{B}}_i \Delta \underline{U}_i = \underline{b}, \quad (28)$$

where  $\tilde{\mathbf{B}}_i$  is a block matrix of the kind  $\tilde{\mathbf{B}}_i = [\mathbf{B}_i, \mathbf{B}_{D,i}]^\top$  and the vector  $\underline{b}$  is of the form  $\underline{b} = [\underline{0}, \underline{b}_D]^\top$  such that  $\mathbf{B}_{D,i}[j, k] = 1$ , if and only if  $k$  is the index of a Dirichlet node  $j$  of the subdomain  $\Omega_i$ , while  $\underline{b}[j]$  equals the Dirichlet values corresponding to the vertices  $\mathbf{X}_k \in \Gamma_{0,D}$ , see also [19].

For three-dimensional elasticity problems all subdomain stiffness matrices have now the same and known defect, which equals the number of six rigid body motions and which also simplifies the calculation of the later needed generalized inverse matrices  $\mathbf{K}_i^\dagger$ . For all-floating FETI we

finally get the linearized system of equations

$$\begin{pmatrix} \mathbf{K}'_1 & & \tilde{\mathbf{B}}_1^\top \\ & \ddots & \vdots \\ & & \mathbf{K}'_p & \tilde{\mathbf{B}}_p^\top \\ \tilde{\mathbf{B}}_1 & \dots & \tilde{\mathbf{B}}_p & \mathbf{0} \end{pmatrix} \begin{pmatrix} \Delta \underline{U}_1 \\ \vdots \\ \Delta \underline{U}_p \\ \underline{\lambda} \end{pmatrix} = \begin{pmatrix} \underline{f}_1 \\ \vdots \\ \underline{f}_p \\ \underline{b} \end{pmatrix}. \quad (29)$$

### 4.3 Solving the FETI system

To solve the linearized systems (27) and (29) we follow the standard approach of tearing and interconnecting methods. For convenience we outline the procedure by means of the classical FETI formulation (Sect. 4.1). However the modulus operandi is analogous for the all-floating approach.

First, note that in the case of a floating subdomain  $\Omega_{0,i}$ , i.e.  $\Gamma_{0,i} \cap \Gamma_{0,D} = \emptyset$ , the local matrices  $\mathbf{K}'_i$  are not invertible. Hence, we introduce a generalized inverse  $\mathbf{K}_i^\dagger$  to represent the local solutions as

$$\Delta \underline{U}_i = \mathbf{K}_i^\dagger (\underline{f}_i - \mathbf{B}_i^\top \underline{\lambda}) + \sum_{k=1}^6 \gamma_{k,i} \underline{r}_{k,i}. \quad (30)$$

Here,  $\underline{r}_{k,i} \in \ker \mathbf{K}'_i$  correspond to the rigid body motions of elasticity. For floating subdomains we additionally require the solvability conditions

$$(\underline{f}_i - \mathbf{B}_i^\top \underline{\lambda}, \underline{r}_{k,i}) = 0 \quad \text{for } i = 1, \dots, 6.$$

In the case of a non-floating subdomain, i.e.  $\ker \mathbf{K}_i = \emptyset$ , we may set  $\mathbf{K}_i^\dagger = \mathbf{K}_i^{-1}$ . In Sect. 4.2 we comment on an all-floating approach where also Dirichlet boundary conditions are incorporated by using discrete Lagrange multipliers.

In general, the Schur complement system of (27) is constructed to obtain

$$\sum_{i=1}^p \mathbf{B}_i \mathbf{K}_i^\dagger \mathbf{B}_i^\top \underline{\lambda} - \sum_{i=1}^p \sum_{k=1}^6 \gamma_{k,i} \mathbf{B}_i \underline{r}_{k,i} = \sum_{i=1}^p \mathbf{B}_i \mathbf{K}_i^\dagger \underline{f}_i, \quad (\underline{f}_i - \mathbf{B}_i^\top \underline{\lambda}, \underline{r}_{k,i}) = 0.$$

This can be formulated clearer as

$$\begin{pmatrix} \mathbf{F} & -\mathbf{G} \\ \mathbf{G}^\top & \mathbf{0} \end{pmatrix} \begin{pmatrix} \underline{\lambda} \\ \underline{\gamma} \end{pmatrix} = \begin{pmatrix} \underline{d} \\ \underline{e} \end{pmatrix}, \quad (31)$$

with

$$\mathbf{F} = \sum_{i=1}^p \mathbf{B}_i \mathbf{K}_i^\dagger \mathbf{B}_i^\top, \quad \mathbf{G} = \sum_{i=1}^p \sum_{k=1}^6 \mathbf{B}_i \underline{r}_{k,i}, \quad \underline{d} = \sum_{i=1}^p \mathbf{B}_i \mathbf{K}_i^\dagger \underline{f}_i,$$

and  $\underline{e}$  constructed using  $e_{k,i} = (\underline{f}_i, \underline{r}_{k,i})$  for  $i = 1, \dots, p$  and  $k = 1, \dots, 6$ . For the solution of the linearized system (31) the projection

$$\mathbf{P}^\top := \mathbf{I} - \mathbf{G} (\mathbf{G} \mathbf{G}^\top)^{-1} \mathbf{G}^\top \quad (32)$$

is introduced. It now remains to consider the projected system

$$\mathbf{P}^\top \mathbf{F} \underline{\lambda} = \mathbf{P}^\top \underline{d}. \quad (33)$$

This can be solved by using a parallel iterative method with suitable preconditioning of the form

$$\mathbf{P}\mathbf{M}^{-1} := \sum_{i=1}^p \mathbf{B}_i \mathbf{Y}_i \mathbf{B}_i^\top. \quad (34)$$

Since the local subproblems all yield symmetric tangent stiffness matrices  $\mathbf{K}'_i$ ,  $i = 1, \dots, p$ , cf. Sect. 3, the matrix  $\mathbf{P}^\top \mathbf{F}$  is also symmetric. This enables us to use the conjugate gradient (CG) method as the global solver for (33). Be aware that the initial approximate solution  $\underline{\lambda}^0$  has to satisfy the compatibility condition  $\mathbf{G}^\top \underline{\lambda}^0 = \underline{e}$ . A possible choice is

$$\underline{\lambda}_0 = \mathbf{G} (\mathbf{G}^\top \mathbf{G})^{-1} \underline{e}.$$

In a post processing we finally recover the vector of constants

$$\gamma = (\mathbf{G}^\top \mathbf{G})^{-1} \mathbf{G}^\top (\mathbf{F}\underline{\lambda} - \underline{d}),$$

and subsequently the desired solution (30).

#### 4.4 Preconditioning

Following Farhat et al. [17] we apply either the lumped preconditioner

$$\mathbf{P}\mathbf{M}^{-1} := \sum_{i=1}^p \mathbf{B}_i \mathbf{K}'_i \mathbf{B}_i^\top, \quad (35)$$

or the optimal Dirichlet preconditioner

$$\mathbf{P}\mathbf{M}^{-1} := \sum_{i=1}^p \mathbf{B}_i \begin{pmatrix} \mathbf{0} & \mathbf{0} \\ \mathbf{0} & \mathbf{S}_i \end{pmatrix} \mathbf{B}_i^\top, \quad (36)$$

where

$$\mathbf{S}_i = \mathbf{K}'_{CC}(\underline{U}_i^k) - \mathbf{K}'_{Ci}(\underline{U}_i^k) \mathbf{K}'_{ii}^{-1}(\underline{U}_i^k) \mathbf{K}'_{iC}(\underline{U}_i^k)$$

is the Schur complement of the local finite element matrix  $\mathbf{K}'_i$ . Alternatively, one may also use scaled hypersingular boundary integral operator preconditioners, as proposed in [43].

## 5 Numerical Results

In this section numerical examples for the finite element tearing and interconnecting approach for linear and nonlinear elasticity problems are presented. First, the FETI implementation is tested within linear elasticity. Here we are able to compare the computed results to a given exact solution. This enables us to show the efficiency of our implementation and also the convergence rates, as predicted from the theory. We compare the different preconditioning techniques and present differences between the classical FETI and the all-floating FETI approach.

Subsequently, we apply the FETI method to nonlinear elasticity problems. Thereby, we focus on the anisotropic model, as described in Sect. 2, and use a realistic triangulations of the aorta and a common carotid artery. As in the linear elastic case, different preconditioning techniques for the all-floating and for the classical FETI method are compared.

The calculations were performed by using the *VSC2*-cluster (<http://vsc.ac.at/>) in Vienna. This Linux cluster features 1314 compute nodes, each with two AMD Opteron Magny Cours 6132HE (8 Cores, 2.2 GHz) processors and 8 x 4 RAM. This yields the total number of 21 024 available processing units. As local direct solver we use Pardiso [44, 45], included in Intel's Math Kernel Library (MKL).

## 5.1 Linear Elasticity

In this section of numerical benchmarks we consider a linear elastic problem with the academic example of a unit cube which is decomposed into a certain number of subcubes. Dirichlet boundary conditions are imposed all over the surface  $\Gamma_D = \partial\Omega$ . The parameters used are Young's modulus  $E = 210$  and Poisson's ratio  $\nu = 0.45$ . The calculated solution is compared to the fundamental solution of linear elastostatics

$$U_{1k}^*(\mathbf{x}, \mathbf{x}^*) = \frac{1}{8\pi} \frac{1+\nu}{E(1-\nu)} \left[ (3-4\nu) \frac{\delta_{1k}}{|\mathbf{x}-\mathbf{x}^*|} + \frac{(x_1-x_1^*)(x_l-x_l^*)}{|\mathbf{x}-\mathbf{x}^*|^3} \right], \quad k = 1, 2, 3 \quad (37)$$

for all  $\mathbf{x} \in \Omega$ ,  $\mathbf{x}^* \in \mathbb{R}^3$  is an arbitrary point outside of the domain  $\Omega$ , and  $\delta_{ij}$  the Kronecker delta, see [46]. The different strategies of preconditioning are compared and also the all-floating and classical FETI approaches. As global iterative method we use the conjugate gradient (CG) method with a relative error reduction of  $\varepsilon = 10^{-8}$ . Under consideration is a linear elasticity problem using linear tetrahedral elements ( $\mathcal{P}_1$ -elements) with a uniform refinement over five levels ( $\ell = 1, \dots, 5$ ) given a cube with 512 subdomains.

Hence, the number of degrees of freedom associated with the coarsest mesh is 9 981 for the all-floating FETI approach and 6 621 for the classical FETI approach. The difference of the numbers is due to the decoupling of the Dirichlet boundary  $\Gamma_D$ . For the finest mesh we have 31 116 861 (all-floating) and 31 073 181 (classical) degrees of freedom. The number of Lagrange multipliers varies between 38 052 for level 1 and 2 908 692 for level 5. Again we have a higher number of Lagrange multipliers for the all-floating approach due to the decoupling of the Dirichlet boundary conditions. The computations were performed on VSC2 using 512 processing units.

First note in Table 2 that for all examined settings, the L2 error, i.e.

$$\|\mathbf{u} - \mathbf{u}_h\|_{L_2(\Omega)}, \quad (38)$$

where  $\mathbf{u}_h$  is the approximate and  $\mathbf{u}$  the exact solution, and the estimated order of convergence

$$\text{eoc}_\ell = \frac{\ln\|\mathbf{u} - \mathbf{u}_{h,\ell}\|_{L_2(\Omega)} - \ln\|\mathbf{u} - \mathbf{u}_{h,\ell-1}\|_{L_2(\Omega)}}{\ln 2} \quad (39)$$

behaves as predicted from the theory, i.e. it is of second order. As expected the least iteration numbers were observed for the optimal Dirichlet preconditioner. Nonetheless, since no additional time is required to compute the lumped preconditioner, in contrast to the more sophisticated Dirichlet preconditioner, this type of preconditioning yields comparable computation times for each level of refinement. As a comparison we also list the results of a very simple preconditioning technique, using the identity matrix for  $\mathbf{Y}_i$  in (34), where almost no reduction of the condition numbers can be noticed.

Moreover, we observe that all-floating FETI yields better condition numbers for all preconditioners, and hence better convergence rates of the global conjugate gradient method. Although the global iterative method converges in less iterations for this approach, we achieve lower computation times for the classical FETI method for the linear elastic case with  $\mathcal{P}_1$ -elements. This is mainly due to the larger expenditure of time to set up the all-floating FETI system, the larger coarse matrix  $\mathbf{G}\mathbf{G}^\top$ , cf. (32), and due to the higher amount of Lagrange multipliers.

From level 4, with a maximum of 8 907 local degrees of freedom, to level 5, with a maximum of 66 195 local degrees of freedom, we observe an increase in the local assembling and factorization time from approximately 1.8 seconds up to about 13 seconds for all kinds of preconditioners. This is mainly due to the higher memory requirements of the direct solver. Note also that the factorization of the local stiffness matrices by the direct solver is unfeasible, if the number of

Table 2: Iteration numbers (it.), condition numbers and computation times (in s) for each preconditioning technique using  $\mathcal{P}_1$ -elements.  $\ell$  is the level of uniform refinement, for the L2 error is the value given in (38) and eoc is the estimated error of convergence.

<b>all-floating</b>											
$\ell$	identity prec.			lumped prec.			Dirichlet prec.			L2 error	eoc
1	61 it.	53.6	20.9 s	27 it.	10.3	19.7 s	21 it.	7.6	19.5 s	1.42e-04	-
2	71 it.	70.0	19.6 s	38 it.	19.7	18.8 s	26 it.	10.4	18.4 s	3.71e-05	1.94
3	88 it.	108.8	21.7 s	45 it.	26.1	22.3 s	27 it.	9.7	22.3 s	9.40e-06	1.98
4	119 it.	216.8	28.8 s	62 it.	53.2	26.4 s	32 it.	13.1	26.6 s	2.37e-06	1.99
5	160 it.	432.7	116.6 s	91 it.	126.2	99.0 s	37 it.	16.8	105.9 s	5.96e-07	1.99
<b>classical</b>											
$\ell$	identity prec.			lumped prec.			Dirichlet prec.			L2 error	eoc
1	80 it.	98.2	7.1 s	35 it.	14.1	5.9 s	29 it.	10.0	5.9 s	1.47e-04	-
2	105 it.	161.4	7.8 s	58 it.	41.9	6.1 s	37 it.	16.4	5.8 s	3.72e-05	1.98
3	140 it.	295.7	9.3 s	85 it.	105.9	7.9 s	46 it.	25.4	7.7 s	9.41e-06	1.98
4	188 it.	580.9	15.2 s	125 it.	252.1	13.1 s	54 it.	35.8	12.2 s	2.37e-06	1.99
5	251 it.	1150.3	103.4 s	179 it.	555.7	88.2 s	60 it.	46.3	83.6 s	5.96e-07	1.99

local degrees of freedom gets too large. The reason for that are memory limitations on the VSC2 cluster. A possibility to overcome this problem is the use of fast local iterative solvers, e.g., the CG method with a multigrid or a BPX preconditioner. Summing it up seems that the simple lumped preconditioner and the classical FETI approach appear to be favorable for this academic example, with very structured subdomains and the boundary  $\Gamma_D = \partial\Omega$ . The latter yields a large number of floating subdomains for all-floating FETI which are non-floating for the classical FETI approach and hence a much larger coarse matrix  $\mathbf{G}\mathbf{G}^\top$  for all-floating FETI. The inversion of this matrix is the most time consuming part for the levels  $\ell = 1, \dots, 4$  what also results in the higher computation times for all-floating FETI in these cases.

Next, we consider a linear elastic problem by using tetrahedral elements and quadratic ansatz functions, i.e.  $\mathcal{P}_2$ -elements for the same mesh and parameter properties as above. The number of degrees of freedom now varies between 53 181 (level  $\ell = 1$ ) and 26 398 269 (level  $\ell = 4$ ) and the number of Lagrange multipliers between 77 700 and 2 908 692. Note that for all preconditioning types and for both the all-floating and the classical FETI method the L2 error compared to the fundamental solution behaves as predicted from the theory as we get a cubic convergence rate, see Table 3.

For all-floating FETI we have the very interesting case that the global CG iteration numbers remain almost constant for the lumped preconditioner, and it even seems to be a decay for the identity and the Dirichlet preconditioner, if we increase the local degrees of freedom, i.e. increase the refinement level  $\ell$ .

For the classical FETI approach the iteration numbers stay almost constant for the Dirichlet preconditioner and increase marginally for the other two preconditioning techniques. Concerning the computation times we have an analogous result as in the previous case with linear ansatz functions: the classical approach with the lumped preconditioner seems to be the best choice for this particular example.

## 5.2 Arterial Model on a Realistic Mesh Geometry

In this section we present examples to show the applicability of the FETI approaches for biomechanical applications, in particular the inflation of an artery segment. We consider the mesh of an aorta and the mesh of a common carotid artery, see Fig. 4 and Fig. 5. The geometries are from AneuriskWeb [47] and Gmsh [48]. The generation of the volume mesh was performed using

Table 3: Iteration numbers (it.), condition numbers and computation times (in s) for each preconditioning technique using  $\mathcal{P}_2$ -elements;  $\ell$  is the level of uniform refinement, L2 error is the value given in (38) and eoc is the estimated error of convergence.

<b>all-floating</b>											
$\ell$	identity prec.			lumped prec.			Dirichlet prec.			L2 error	eoc
1	149 it.	444.7	23.3 s	73 it.	73.7	22.0 s	47 it.	36.7	18.7 s	1.13e-05	-
2	129 it.	330.8	21.9 s	75 it.	74.3	20.8 s	43 it.	27.7	19.3 s	1.44e-06	2.97
3	114 it.	210.3	30.3 s	73 it.	68.8	27.3 s	36 it.	16.6	28.5 s	1.81e-07	2.99
4	105 it.	167.8	99.8 s	69 it.	65.2	93.4 s	33 it.	14.4	90.2 s	2.26e-08	3.00
<b>classical</b>											
$\ell$	identity prec.			lumped prec.			Dirichlet prec.			L2 error	eoc
1	120 it.	405.0	7.5 s	65 it.	48.9	6.9 s	40 it.	21.0	6.5 s	1.17e-05	-
2	108 it.	302.6	7.5 s	69 it.	57.6	6.7 s	41 it.	20.6	7.5 s	1.46e-06	3.00
3	112 it.	253.4	12.6 s	91 it.	116.2	11.7 s	42 it.	21.0	12.3 s	1.82e-07	3.01
4	136 it.	273.1	76.3 s	128 it.	262.8	77.3 s	48 it.	27.7	79.1 s	2.26e-08	3.01

VMTK and Gmsh [48].

The fiber directions, see Fig. 6, were calculated using a method described by Bayer et al. [49] for the myocardium. To adapt this method for the artery we first solved the Laplace equation on the domain  $\Omega_0$  with homogeneous Dirichlet boundary conditions on the inner surface and inhomogeneous Dirichlet boundary conditions on the outer wall. The gradient of the solution is used to define the transmural direction  $\hat{\mathbf{e}}_2$  in each element. As a second step we repeat this procedure using homogeneous Dirichlet boundary conditions on the inlet surface and inhomogeneous boundary conditions on the outlet surfaces which yields the longitudinal direction  $\hat{\mathbf{e}}_1$ . The cross product of these two vectors eventually provides the circumferential direction  $\hat{\mathbf{e}}_0$ . With a rotation we get the two desired fiber directions  $\mathbf{a}_{0,1}$  and  $\mathbf{a}_{0,2}$  in the media and the adventitia, respectively. Thus,

$$(\mathbf{a}_{0,1} \quad -\mathbf{a}_{0,2} \quad \hat{\mathbf{e}}_2) = (\hat{\mathbf{e}}_0 \quad \hat{\mathbf{e}}_1 \quad \hat{\mathbf{e}}_2) \begin{pmatrix} \cos \alpha & -\sin \alpha & 0 \\ \sin \alpha & \cos \alpha & 0 \\ 0 & 0 & 1 \end{pmatrix} \begin{pmatrix} \hat{\mathbf{e}}_0^\top \\ \hat{\mathbf{e}}_1^\top \\ \hat{\mathbf{e}}_2^\top \end{pmatrix} (\hat{\mathbf{e}}_0 \quad \hat{\mathbf{e}}_1 \quad \hat{\mathbf{e}}_2). \quad (40)$$

The values for the angle  $\alpha$  are  $\alpha_M = 29^\circ$  for the media and  $\alpha_A = 62^\circ$  for the adventitia, taken from [5].

To describe the anisotropic and nonlinear cardiac tissue, we use the material model (9)–(13), with the parameters given in Table 1 and  $\kappa$  is varied. Dirichlet boundary conditions (4) are imposed on the respective intersection areas. We perform an inflation simulation on the artery segment where the interior wall is exposed to a constant pressure  $p$ . This is performed using Neumann boundary conditions (5). If not stated otherwise, we present the results of one load step applying a rather low pressure of 1 mmHg. This is necessary to have a converging Newton method. Nonetheless, the material model as used is anisotropic. To simulate a higher pressure, an appropriate load stepping scheme, see (19), has to be used. However, this does not affect the number of local iterations significantly. As already mentioned in Sect. 4 we use the CG method as global iterative solver. Experiments with a standard non-symmetric nonlinear elasticity system and the hence necessary GMRES method as an iterative solver showed similar results as presented in the following with the symmetric system. However, the memory requirements of the GMRES solver are much higher.

The local generalized pseudo-inverse matrices are realized with a sparsity preserving regularization and the direct solver package Pardiso. The global nonlinear finite element system is solved by a Newton scheme, where the FETI approach is used in each Newton step. For the

considered examples the Newton scheme needed four to six iterations. Due to the non-uniformity of the subdomains the efficiency of a global preconditioner becomes more important. It can happen that the decomposition of a mesh results in subdomains that have only a few points on the Dirichlet boundary. This negatively affects the convergence of the CG method using classical FETI, but does not affect the global iterative method of the all-floating approach at all. This is a major advantage of all-floating FETI since here all subdomains are treated the same and hence all subdomains are stabilized. This behavior is observed for almost all settings for preconditioners and the penalty parameter  $\kappa$  as well as for linear and quadratic ansatz functions, see Table 4, Table 5 Table 6 and Table 7. For instance, applying all-floating FETI with the Dirichlet

Table 4: Iteration numbers (it.) per Newton step and computation times (in s) per Newton step for the all-floating and the classical FETI approach with *linear* ansatz functions comparing the three considered preconditioners. The penalty parameter  $\kappa$  was varied from 10 to 1000 kPa. Mesh: mesh of the aorta subdivided in 480 subdomains, computed with 480 cores.

<b>all-floating</b>						
$\kappa$	identity prec.		lumped prec.		Dirichlet prec.	
10	1052 it.	57.6 s	160 it.	31.0 s	56 it.	22.8 s
100	1879 it.	94.6 s	305 it.	29.5 s	85 it.	25.4 s
1000	4122 it.	177.1 s	681 it.	48.8 s	209 it.	31.8 s
<b>classical</b>						
$\kappa$	identity prec.		lumped prec.		Dirichlet prec.	
10	2056 it.	98.7 s	305 it.	35.5 s	117 it.	27.2 s
100	3711 it.	149.8 s	540 it.	35.5 s	144 it.	28.4 s
1000	8245 it.	327.8 s	1190 it.	60.9 s	263 it.	32.9 s

Table 5: Iteration numbers (it.) per Newton step and computation times (in s) per Newton step for the all-floating and the classical FETI approach with *linear* ansatz functions comparing the three considered preconditioners. The penalty parameter  $\kappa$  was set to 1000 kPa. Mesh: mesh of the carotis with two layers (adventitia and media) subdivided in 512 subdomains, computed with 512 cores.

type	identity prec.		lumped prec.		Dirichlet prec.	
all-floating	> 10000 it.	- s	1084 it.	100.6 s	497 it.	85.5 s
classical	5130 it.	357 s	1794 it.	200.2 s	588 it.	97.7 s

preconditioner to the aorta mesh using a penalty parameter  $\kappa = 1000$  the global CG method converged in considerable less iterations (209) than the CG method using classical FETI (263), see Table 4. The advantage of the smaller number of iterations is not so significantly reflected in the computation times since, as for the linear case, we have higher set up times and a larger coarse system  $\mathbf{GG}^\top$ . Nonetheless, it shows for the considered examples that all-floating FETI yields lower iterations numbers of the global systems and is also competitive or even advantageous to the classical approach concerning the computation times.

In contrast to the academic example in Sect. 5.1 the more complex Dirichlet preconditioner is the best choice for all considered settings. Especially for  $\kappa \gg 1$  the iteration numbers with the lumped and the identity preconditioner escalate. Admittedly, the numbers in Table 4 also show that the convergence of the CG method, within all FETI approaches and preconditioner settings, is dependent on the penalty parameter  $\kappa$ .

Using quadratic ansatz functions we have a total number of 23 031 620 d.o.f. for the aorta mesh and 36 527 435 d.o.f. for the carotis mesh. In order to not infringe the memory limitations

Table 6: Iteration numbers (it.) per Newton step and computation times (in s) per Newton step for the all-floating and the classical FETI approach with *quadratic* ansatz functions comparing the three considered preconditioners. The penalty parameter  $\kappa$  was varied from 10 to 1000 kPa. Mesh: mesh of the aorta subdivided in 480 subdomains, calculated with 480 cores.

<b>all-floating</b>						
$\kappa$	identity prec.		lumped prec.		Dirichlet prec.	
10	940 it.	491.1 s	283 it.	209.5 s	71 it.	157.3 s
100	1519 it.	1186.4 s	523 it.	332.0 s	105 it.	178.1 s
1000	3371 it.	2584.5 s	1372 it.	746.0 s	206 it.	282.7 s
<b>classical</b>						
$\kappa$	identity prec.		lumped prec.		Dirichlet prec.	
10	1319 it.	654.2 s	333 it.	225.2 s	113 it.	188.4 s
100	2362 it.	1140.6 s	664 it.	402.6 s	110 it.	177.5 s
1000	5563 it.	4168.3 s	1742 it.	943.1 s	204 it.	280.1 s

Table 7: Iteration numbers (it.) per Newton step and computation times (in s) per Newton step for the all-floating and the classical FETI approach with *quadratic* ansatz functions comparing the three considered preconditioners. The penalty parameter  $\kappa$  was set to 1000 kPa. Mesh: mesh of the carotis with two layers (adventitia and media) subdivided in 1024 subdomains, calculated with 1024 cores.

type	identity prec.		lumped prec.		Dirichlet prec.	
all-floating	> 10000 it.	- s	2163 it.	1133.9 s	674 it.	994.6 s
classical	6006 it.	2672.6 s	4798 it.	2306.8 s	764 it.	771.2 s

on the *VSC2* cluster we have to use a decomposition into 1024 subdomains for the carotis. For the aorta it was possible to stay with 480 subdomains. The number of Lagrange multipliers then are 1 552 665 (aorta) and 4 585 203 (carotis). Comparing the numbers in Table 6 and Table 7 show similar results as in the case with linear ansatz functions. The Dirichlet preconditioner is preferable for all test cases and the all-floating approach is competitive to the classical FETI approach. Albeit quadratic ansatz functions resolve the nearly incompressible elastic behavior better than linear ansatz functions we also notice a certain dependence of the global iteration numbers to the penalty parameter  $\kappa$ , see Table 6. Nonetheless, the iteration numbers rise not as quickly as for the  $P_1$ - $P_0$ -element case and the values of  $J = \det(\mathbf{F})$  in each element are much closer to 1 for  $P_2$ - $P_0$ -elements.

### 5.3 Strong Scaling for Nonlinear Elasticity

We consider the meshes of the carotid artery and the aorta as in Section 5.2, both subdivided into 512 subdomains. We apply the arterial model with the parameters from Table 1 and  $\kappa = 100$  using the lumped preconditioner and linear ansatz functions. For the aorta we used all-floating FETI and needed an average of 324 global CG iterations to reach an absolute error of  $\varepsilon = 10^{-8}$  and 5 Newton steps to reach an absolute error of  $10^{-6}$ . In the case of the carotis and classical FETI we needed 674 global CG iterations and also 5 Newton steps to reach the same error limits as above.

In Table 8 and Table 9 we present the following numbers: the *local time* is the sum of all assembling and local factorization times during the solution steps. The factorization of the local problems was done with the direct solver package Pardiso. In most cases we observe a super-linear speedup and hence an efficiency greater than 1 for this value. This is due to memory issues, mainly so-called cache effects. The *global CG time* is the duration of all CG solution

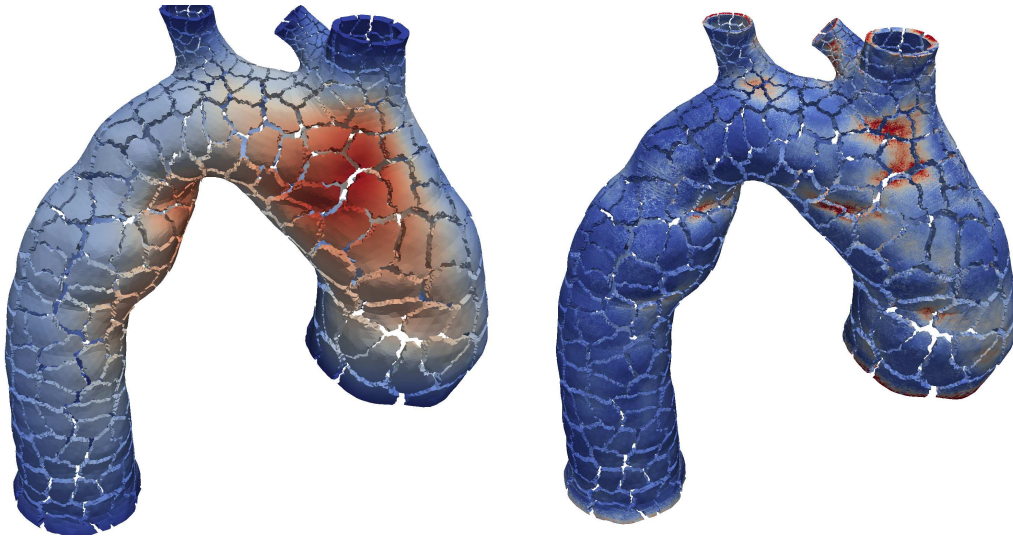


Figure 4: Mesh of an aorta consisting of 5 418 594 tetrahedrons and 1 055 901 vertices. Point of view is from above showing the links to the brachiocephalic, the left common carotid and the left subclavian artery. Colors indicate the displacement field (left) and the von Mises stress (right) generated by applying a pressure to the inner walls of the arteries. Red colors indicate high, blue colors indicate low displacement or stress respectively. Additionally, the splits show the decomposition of the mesh into 480 subdomains.

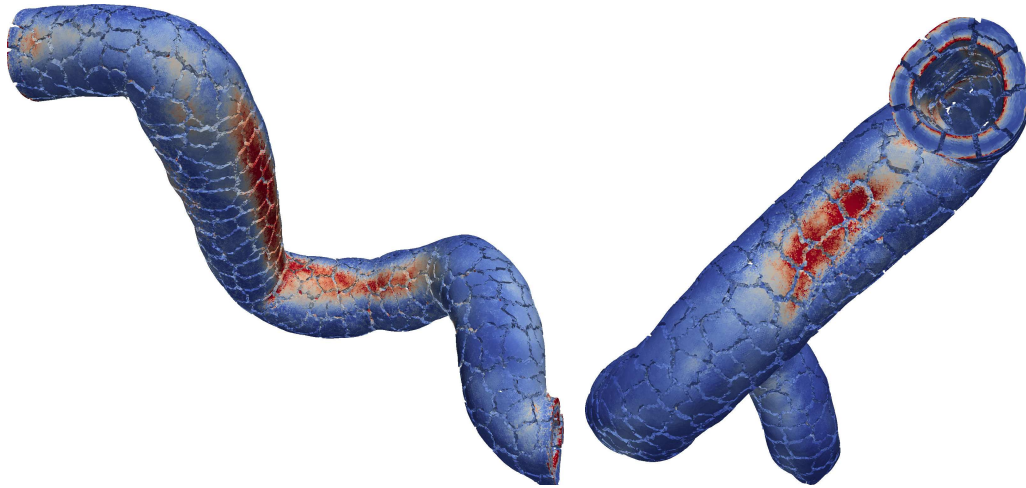


Figure 5: Mesh of a segment of a common carotid artery from two different points of view. The mesh consists of 9 195 336 tetrahedrons and 1 621 365 vertices. Colors indicate the von Mises stress field generated by applying a pressure to the inner walls of the artery. Red colors indicate high, blue colors indicate low stress/displacement. Additionally, the splits show the decomposition of the mesh into 512 subdomains.

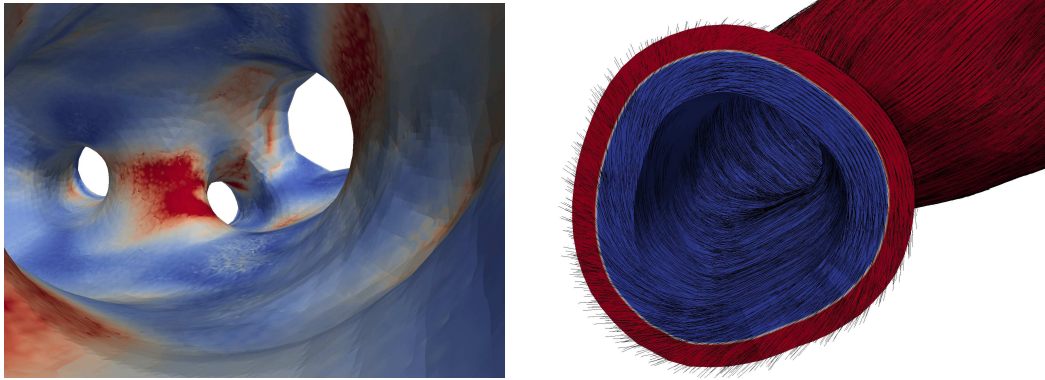


Figure 6: Von Mises stress looking inside the aorta (left); values of high von Mises stress in red and of low stress in blue. To the right the fiber directions (black lines) and the two layers (adventitia in red and media in blue) of the carotis are shown

Table 8: Computational times (in s) and efficiency (eff.) for a nonlinear elastic problem using a varying number of processing units  $p$ . The time is measured for 1 time step with 5 Newton steps for allfloating FETI and the lumped preconditioner

$p$	local time	eff.	global CG time	eff.	total time	eff.
16	407.7 s	-	1311.7 s	-	2028.6 s	-
32	203.1 s	1.004	666.4 s	0.984	1054.2 s	0.962
64	101.7 s	1.002	345.4 s	0.949	562.0 s	0.902
128	50.5 s	1.009	184.7 s	0.888	316.7 s	0.801
256	25.3 s	1.007	103.8 s	0.790	192.8 s	0.658
512	12.7 s	1.000	67.6 s	0.606	161.0 s	0.394

steps together. We see that this value scales very good up to 256 cores for the aorta and up to 128 cores for the carotis. The *total time* is the total computation time including input and output functions. It also scales admissibly well up to 256 processing units for the aorta and up to 128 cores for the carotis, see Table 8, Table 9 and Fig. 7. For a higher number of cores, at least for the specific examples, the speedup is rather low. Possibilities to overcome this problem are for example the usage of parallel solver packages as *hypre* and a more efficient assembling of the coarse system of the FETI method. It also will need a more elaborate strategy with MPI and the memory management. Note that at some point the subdomains get too small and the increasingly dominant MPI communication impedes further strong scaling.

Table 9: Computational times (in s) and efficiency (eff.) for a nonlinear elastic problem on the carotis mesh using a varying number of processing units  $p$ . The time is measured for 1 time steps with 5 Newton steps for classical FETI and the lumped preconditioner.

$p$	local time	eff.	global CG time	eff.	total time	eff.
16	726.0 s	-	4725.8 s	-	6519.7 s	-
32	351.3 s	1.033	2368.2 s	0.998	3497.0 s	0.932
64	170.5 s	1.065	1262.9 s	0.936	1991.2 s	0.819
128	90.7 s	1.001	694.5 s	0.851	1194.1 s	0.682
256	47.3 s	0.960	443.6 s	0.666	914.4 s	0.446
512	23.9 s	0.949	297.2 s	0.497	667.4 s	0.305

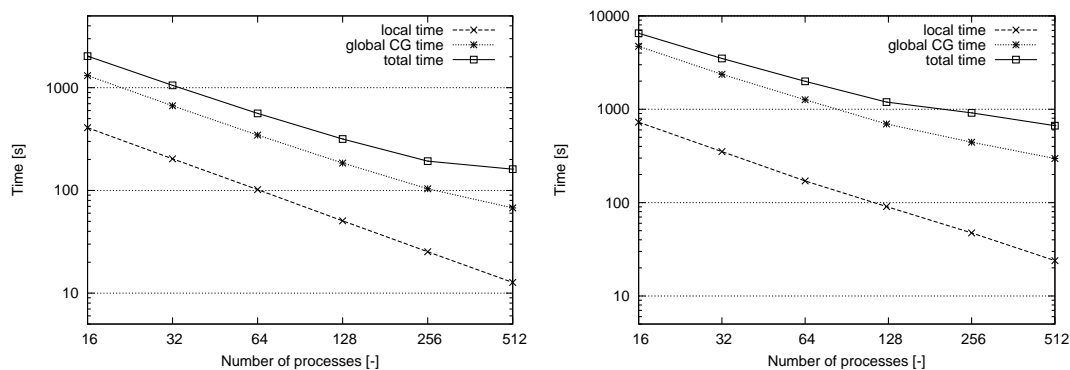


Figure 7: Computation times (in s) for a simulation of the anisotropic arterial model with the aorta mesh (left) and the carotis mesh (right) using a varying number of cores.

## 6 Discussion and Limitations

We have shown the application of the finite element tearing and interconnecting method to elasticity problems, in particular to the simulation of the nonlinear elastic behavior of cardiovascular tissues such as the artery. The main ideas of domain decomposition methods were summarized and the classical and the all-floating FETI approach were discussed in detail.

Illustrated by numerical examples we have shown certain advantages of the all-floating FETI method compared to the classical FETI approach. To the best of our knowledge the application of the all-floating approach to nonlinear anisotropic elasticity problems cannot be found in the

literature. For sure the mentioned advantages are influenced by the mesh structure and the choice of the boundary conditions, and hence the method to choose depends on the specific problem.

We have presented and compared different techniques of preconditioning: the lumped preconditioner and the optimal Dirichlet preconditioner. Furthermore, the numerical examples exposed some instabilities of the global iterative method for nearly incompressible material parameters, i.e. for a very large penalty parameter  $\kappa$ . Here we were able to present, like it was also shown in earlier contributions, that quadratic ansatz functions resolve the incompressible elastic behavior better than linear ansatz functions.

## Acknowledgements

This work was supported by the Austrian Science Fund (FWF) and Graz University of Technology within the SFB Mathematical Optimization and Applications in Biomedical Sciences. The authors would like to thank Dr. Günther Of, Graz University of Technology and Dr. Clemens Pechstein, Johannes Kepler University of Linz, for the fruitful cooperation and many helpful discussions.

## References

- [1] Ciarlet PG. *Mathematical elasticity. Vol. I, Studies in Mathematics and its Applications*, vol. 20. North-Holland: Amsterdam, 1988.
- [2] Holzapfel GA. *Nonlinear Solid Mechanics. A Continuum Approach for Engineering*. John Wiley & Sons Ltd: Chichester, 2000.
- [3] Marsden JE, Hughes TJR. *Mathematical Foundations of Elasticity*. Dover: New York, 1994.
- [4] Ogden RW. *Non-linear Elastic Deformations*. Dover: New York, 1997.
- [5] Holzapfel GA, Gasser TC, Ogden RW. A new constitutive framework for arterial wall mechanics and a comparative study of material models. *J. Elasticity* 2000; **61**:1–48.
- [6] Holzapfel GA, Ogden RW. Constitutive modelling of arteries. *Proc. R. Soc. Lond. Ser. A Math. Phys. Eng. Sci.* 2010; **466**(2118):1551–1596.
- [7] Gasser TC, Ogden RW, Holzapfel GA. Hyperelastic modelling of arterial layers with distributed collagen fibre orientations. *J. R. Soc. Interface* 2006; **3**:15–35.
- [8] Holzapfel GA. Collagen in arterial walls: Biomechanical aspects. *Collagen. Structure and Mechanics*, Fratzl P (ed.). chap. 11, Springer-Verlag, 2008; 285–324.
- [9] Holzapfel GA, Ogden RW. Modelling the layer-specific 3D residual stresses in arteries, with an application to the human aorta. *Journal of the Royal Society Interface* 2010; **7**:787–799.
- [10] Holzapfel GA, Ogden RW. Constitutive modelling of passive myocardium: a structurally based framework for material characterization. *Phil. Trans. R. Soc. A* 2009; **367**:3445–3475.
- [11] Proceedings of the International Conference on Domain Decomposition Methods in Science and Engineering, vol. I–XXI. <http://www.ddm.org/>.
- [12] Steinbach O. *Stability estimates for hybrid coupled domain decomposition methods, Lecture Notes in Mathematics*, vol. 1809. Springer-Verlag: Berlin, 2003.

- [13] Bernardi C, Maday Y, Patera AT. A new nonconforming approach to domain decomposition: the mortar element method. *Nonlinear partial differential equations and their applications. Collège de France Seminar, Vol. XI (Paris, 1989–1991), Pitman Res. Notes Math. Ser.*, vol. 299. Longman Sci. Tech.: Harlow, 1994; 13–51.
- [14] Maday Y, Mavriplis C, Patera AT. Nonconforming mortar element methods: application to spectral discretizations. *Domain decomposition methods (Los Angeles, CA, 1988)*. SIAM: Philadelphia, PA, 1989; 392–418.
- [15] Wohlmuth BI. A mortar finite element method using dual spaces for the Lagrange multiplier. *SIAM J. Numer. Anal.* 2000; **38**(3):989–1012.
- [16] Farhat C, Roux FX. A method of finite element tearing and interconnecting and its parallel solution algorithm. *Int. J. Numer. Methods Engrg.* 1991; **32**:1205–1227.
- [17] Farhat C, Mandel J, Roux FX. Optimal convergence properties of the FETI domain decomposition method. *Comput. Methods Appl. Mech. Engrg.* 1994; **115**:365–385.
- [18] Of G. *Beti-gebietszerlegungsmethoden mit schnellen randelementverfahren und anwendungen*. PhD Thesis, Universität Stuttgart 2006.
- [19] Of G, Steinbach O. The all-floating boundary element tearing and interconnecting method. *J. Numer. Math.* 2009; **17**(4):277–298.
- [20] Dostál Z, Horák D, Kučera R. Total FETI - an easier implementable variant of the FETI method for numerical solution of elliptic PDE. *Comm. Numer. Methods Engrg.* 2006; **22**:1155–1162.
- [21] Farhat C, Lesoinne M, LeTallec P, Pierson K, Rixen D. FETI-DP: a dual-primal unified FETI method. I. A faster alternative to the two-level FETI method. *Int. J. Numer. Methods Engrg.* 2001; **50**(7):1523–1544.
- [22] Klawonn A, Widlund OB. FETI and Neumann-Neumann iterative substructuring methods: connections and new results. *Comm. Pure Appl. Math.* 2001; **54**(1):57–90.
- [23] Klawonn A, Widlund OB. Selecting constraints in dual-primal FETI methods for elasticity in three dimensions. *Domain decomposition methods in science and engineering, Lect. Notes Comput. Sci. Eng.*, vol. 40. Springer: Berlin, 2005; 67–81.
- [24] Klawonn A, Rheinbach O. Highly scalable parallel domain decomposition methods with an application to biomechanics. *ZAMM Z. Angew. Math. Mech.* 2010; **90**(1):5–32.
- [25] Rheinbach O. Parallel iterative substructuring in structural mechanics. *Arch. Comput. Methods Eng.* 2009; **16**(4):425–463.
- [26] Klawonn A, Widlund OB. A domain decomposition method with Lagrange multipliers and inexact solvers for linear elasticity. *SIAM J. Sci. Comput.* 2000; **22**(4):1199–1219.
- [27] Mandel J, Tezaur R. Convergence of a substructuring method with Lagrange multipliers. *Numer. Math.* 1996; **73**(4):473–487.
- [28] Flory PJ. Thermodynamic relations for high elastic materials. *Trans. Faraday Soc.* 1961; **57**:829–838.

- [29] Coleman BD, Noll W. The thermodynamics of elastic materials with heat conduction and viscosity. *Archive for Rational Mechanics and Analysis* 1963; **13**:167–178.
- [30] Truesdell C, Toupin RA. The classical field theories. *Encyclopedia of Physics*, vol. III/1, Flügge S (ed.). Springer-Verlag: Berlin, 1960; 226–793.
- [31] Rivlin RS, Ericksen JL. Stress-deformation relations for isotropic materials. *J. Ration. Mech. Anal.* 1955; **4**:323–425.
- [32] Raoult A. Symmetry groups in nonlinear elasticity: An exercise in vintage mathematics. *Communications on Pure and Applied Analysis* 2009; **8**(1):435–456.
- [33] Holzapfel GA, Gasser TC, Ogden RW. Comparison of a multi-layer structural model for arterial walls with a fung-type model, and issues of material stability. *J. Biomech. Eng.* 2004; **126**:264–275.
- [34] Ball JM. Constitutive inequalities and existence theorems in nonlinear elastostatics. *Non-linear analysis and mechanics: Heriot-Watt Symposium (Edinburgh, 1976), Vol. I*. Pitman: London, 1977; 187–241. Res. Notes in Math., No. 17.
- [35] Ball JM. Convexity conditions and existence theorems in nonlinear elasticity. *Arch. Rational Mech. Anal.* 1977; **63**(4):337–403.
- [36] Dacorogna B. *Direct methods in the calculus of variations, Applied Mathematical Sciences*, vol. 78. Second edn., Springer: New York, 2008.
- [37] Balzani D, Neff P, Schröder J, Holzapfel GA. A polyconvex framework for soft biological tissues. adjustment to experimental data. *Int. J. of Solids and Structures* 2006; **43**:6052–6070.
- [38] Augustin CM. Classical and all-floating feti methods with applications to biomechanical models. PhD Thesis, Graz University of Technology 2012.
- [39] Holzapfel GA. Structural and numerical models for the (visco)elastic response of arterial walls with residual stresses. *Biomechanics of Soft Tissue in Cardiovascular Systems*, Holzapfel GA, Ogden RW (eds.). Springer: Wien, New York, 2003.
- [40] Boffi D, Brezzi F, Fortin M. Finite elements for the Stokes problem. *Lecture Notes in Mathematics* 2008; **1939**:45–100.
- [41] Pechstein C. *Finite and Boundary Element Tearing and Interconnecting Solvers for Multi-scale Problems, Lecture Notes in Computational Science and Engineering*, vol. 90. Springer, 2013.
- [42] Toselli A, Widlund OB. *Domain Decomposition Methods – Algorithms and Theory*. Springer: Berlin, Heidelberg, 2005.
- [43] Langer U, Steinbach O. Boundary element tearing and interconnecting methods. *Computing* 2003; **71**(3):205–228.
- [44] Schenk O, Bollhöfer M, Römer RA. On large scale diagonalization techniques for the Anderson model of localization. *SIAM Review* 2008; **50**(1):91–112. SIGEST Paper.
- [45] Schenk O, Wächter A, Hagemann M. Matching-based preprocessing algorithms to the solution of saddle-point problems in large-scale nonconvex interior-point optimization. *Comput. Optim. Appl.* 2007; **36**(2-3):321–341.

- 
- [46] Steinbach O. *Numerical approximation methods for elliptic boundary value problems*. Springer: New York, 2008. Finite and boundary elements, Translated from the 2003 German original.
- [47] Aneurisk-Team. AneuriskWeb project website, <http://ecm2.mathcs.emory.edu/aneuriskweb> 2012.
- [48] Geuzaine C, Remacle JF. Gmsh: a three-dimensional finite element mesh generator with built-in pre- and post-processing facilities. *Int. J. Numer. Methods Engrg.* 2009; **79**(11):1309–1331.
- [49] Bayer JD, Blake R, Plank G, Trayanova NA. A novel rule-based algorithm for assigning myocardial fiber orientation to computational heart models. *Ann. Biomed. Eng.* 2012; **40**(10):2243–2254.